RESEARCH ARTICLE

Automated Debonding Characterization in Reinforced Structures Based on Finite Element Analysis and Convolutional Neural Networks

JI-YUN KIM [1], **YOUNGKI KIM** [2], **(Senior Member, IEEE),**
AND JE-HEON HAN [1], **(Member, IEEE)**

[1]Department of Mechanical Engineering, Tech University of Korea, Siheung-si, Gyeonggi-do 15073, South Korea
[2]Department of Mechanical Engineering, University of Michigan–Dearborn, Dearborn, MI 48128, USA

Corresponding author: Je-Heon Han (jeep2000@tukorea.ac.kr)

ABSTRACT A study utilizing convolutional neural networks (CNN) has been conducted to detect and classify invisible debonding-type defects in reinforced structures. Training data for these defects is collected from the finite element models of honeycomb sandwich panels and skin-stringer systems, commonly employed reinforcement structures in aerospace applications. The excitation frequency is determined based on the amplitude of the reflected wave from the defect, and the optimal sensor array is selected. The constructed two-dimensional training image, created by vertically stacking the measured responses in the time domain, exhibits high classification performance even with a shallow neural network. The neural network undergoes optimization through adjustment to the kernel parameters and initial learning rate. To assess the general performance of the training model, k-fold cross-validation is employed. The CNN-based non-destructive evaluation algorithm demonstrates high classification performance for debonding defects in honeycomb sandwich panels and skin-stringer structures. Moreover, the suggested algorithm is robust against noise, emphasizing its effectiveness in real-world applications.

INDEX TERMS CNN, FEA, nondestructive testing, ultrasonic transducer arrays.

I. INTRODUCTION

Honeycomb sandwich and skin-stringer structures are reinforcing structures commonly used in aerospace structures such as wings, engine covers, and fuselages because they have high mechanical strength and are lightweight. These structures consist of thin panels (skin, face sheet) and stiffeners (stringer, core), which work together to minimize deformation and buckling caused by external forces. As defects in these structures are often challenging to detect

The associate editor coordinating the review of this manuscript and approving it for publication was Riccardo Carotenuto.

with the naked eye, non-destructive evaluation becomes essential to identify the presence and location of defects accurately, ensuring overall stability and reliability [1].

In delicate surface structures such as semiconductors, surface characteristics are mainly visualized using secondary electrons (SEs) to profile dopants, or defects are non-destructively evaluated by improving spatial resolution using a scanning helium ion microscope (SHIM). Meanwhile, the most commonly used non-destructive evaluation methods for detecting structural defects in mechanical systems are pulse-echo [2], [3], [4] and through transmission [5], [6]. These methods detect defects by transmitting ultrasonic bulk waves
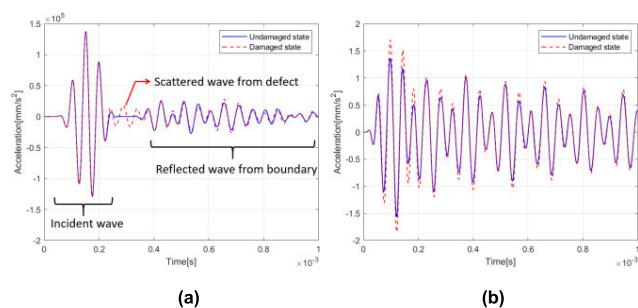
FIGURE 1. An example of comparison of measured signals with and without a structural defect for (a) an aluminum panel, (b) a honeycomb sandwich panel.

to a local area of the test object and analyzing the reflected or transmitted signal. While they offer efficient defect detection in small areas, they suffer from the drawback of being time-consuming when inspecting large objects.

For thin structures, many studies have been conducted using guided waves, which can cover larger areas without the time-consuming transducer-scanning process [7], [8], [9]. Lamb waves are a combination of longitudinal and transverse waves propagating in a traction-force-free plate [10]. Lamb waves can travel long distances with a small energy loss and demonstrate high sensitivity to tiny defects. However, sophisticated digital signal processing techniques are required due to the complex scattering characteristics attributed to the existence of multiple modes (symmetric and anti-symmetric modes) and their dispersion relations [11]. For instance, Alleyne and Cawley [12] conducted a sensitivity analysis of Lamb waves for various defects in the frequency domain using 2D FFT, quantifying the correlation between Lamb wave wavelength and detectable defect size. Han and Kim [13] employed time-frequency Multiple Signal Classification (MUSIC) to continuously identify defects on plates, achieving improved spatial resolution by considering structural damping. Ing and Fink [14] were able to detect structural damages by achieving self-focusing and time compression of the dispersive Lamb waves by correcting the complex dispersion effect of the Lamb wave with a time reversal mirror. Moreover, the interaction between Lamb waves and structural defects was investigated in the time-frequency domain using signal processing techniques, including Short-Time Fourier Transform (STFT) [15], [16], Matching Pursuit [17], [18], Wavelet Transform [19], [20], and Wigner-Ville Transform [21], [22]. These techniques have been successfully applied not only to plates but also to pipelines [23], [24], beams [25], [26], and cables [16] to characterize defects.

On the other hand, interpretation of the measured signal in a honeycomb sandwich or skin-stringer structure, using the signal processing techniques, poses a significant challenge. This is primarily due to the complex nature of multi-mode generation and scattering caused by numerous discontinuous boundaries. For example, in the case of a simple aluminum plate, it is easy to observe the reflected signal from a defect,

as shown in Fig. 1(a). But in the case of a honeycomb sandwich structure composed of an aluminum core and a CFRP skin, as shown in Fig. 1(b), it is difficult to identify the signal associated with a debonding region because of the large number of reflected waves from the junctions between the skin and core.

To address the challenge of analyzing the measured waves in structures with multiple discontinuous boundaries, many studies have been conducted to investigate the Lamb wave propagation characteristics analytically and experimentally [27], [28], [29], [30], [31]. Chakraborty et al. [32] and Zheng et al. [33] utilized the Time of Flight (ToF) of the S0 mode, known for its faster and less dispersive nature than the A0 mode, to estimate the debonding location in the reinforced structure. Sikdar and Banerjee [34] calculated the amplitude change of the A0 mode, which is larger than that of the S0 mode, in a honeycomb sandwich structure with debonding. They visualized the debonding position with a 3D signal difference coefficient (SDC) map. In another approach, Gao et al. [35] evaluated the debonding of the honeycomb sandwich panel through the energy loss and time delay of coda waves using chirp signals. Yashiro et al. [36] presented moving diagrams of the S0 and A0 modes to visualize the debonding location in a skin-stringer structure.

These methods for evaluating the debonding region in stiffened structures by analyzing specific wave components in such a complex measured response are applicable when the wave propagation and reflection characteristics of the structures are thoroughly investigated. However, in real-world structures where various interactions exist, there may be challenges in achieving high accuracy or obtaining reliable results. In order to address these issues, there is a growing interest in developing non-destructive evaluation algorithms applying deep learning techniques [37]. One such method is supervised learning, an algorithm that labels, learns, and provides prediction results for new data [38]. De Fenze et al. [39] used an artificial neural network to predict the location and size of defects in a composite plate by learning the damage index, which calculated the change of the Lamb wave according to the defect. Virupakshappa and Oruklu [40] achieved high classification accuracy by employing Split Spectrum Processing (SSP) decomposition with A-scan data and a Support Vector Machine (SVM) classifier to detect the presence of holes in a steel block. When a plate structure with a defect is excited, the energy level difference according to the defect's location [41], the frequency domain response of the direct wave passing through the defect [42], the time domain response of the reflected wave from the defect [43], and the damage index [44] were imaged in 2D for training. Then Convolutional Neural Network (CNN) effectively classified the defect's location. CNN is specialized for image classification that can effectively learn spatial patterns and operates robustly even under noisy conditions [45].

The CNN-based non-destructive evaluation using guided ultrasound, as proposed in this study, offers several advantages for structural health monitoring. The processing speed

of data is rapid, utilizing raw signals obtained from a sensor array. Moreover, cost-effective maintenance is feasible as ultrasonic measurement equipment is relatively inexpensive and portable. In contrast to other non-destructive testing (NDT) methods like liquid penetrant testing or thermal imaging, this approach exhibits sensitivity to a diverse range of defect types and can effectively detect defects.

This paper presents a method for converting debonding-related signals in stiffened structures into 2D images and subsequently identifying the location and size of debonding regions using a CNN algorithm. Reflected waves are generated when the propagated Lamb wave in the stiffened structure encounters discontinuities such as stiffener boundaries, panel edges, and debonding boundaries. At this time, the wave newly generated or distracted in the debonding area becomes a valuable clue in finding the location or size of the debonding region. To generate the necessary data for debonding classification, each response is measured while moving the debonding position and changing the debonding size. Then, the response is matched with its associated defect location and size through supervised learning. In order to obtain a robust training model, a sufficient amount of training data is essential to avoid overfitting [46]. However, collecting various experimental data is challenging since samples must be produced as many as the type and location of defects. Therefore, to overcome this limitation, Finite Element (FE) analysis is utilized to evaluate the validity of the proposed method, and various training data are collected through the simulation to assess its effectiveness. The main contributions of this research are summarized as follows:

1) Proposing a method to determine the optimal excitation and sensor positions for identifying defects in realistic stiffened structures such as skin-stringers and honeycomb sandwich panels.

2) Suggesting a reliable non-destructive evaluation method by training data in the time domain.

3) Evaluating the proposed method's robustness against measurement error and defect size.

II. METHOD
A. CLASSIFICATION PROCEDURE

The overall process of classifying structural defects is illustrated in Fig. 2. At first, the model, including the structural defect, is excited with the Lamb wave. Subsequently, the scattering response of the Lamb wave passing through the structural defect is measured with the lead zirconate titanate (PZT) sensor array. Measured responses are converted into color bands by assigning different colors according to the amplitude of the response in the time domain and converted into a single image by laying them in the vertical direction [43]. This resultant image is stored in a folder labeled with the respective location of the structural defect, for instance, "debonding location#1", to match the debonding location and its response. Then, this process is repeated while moving the position of the structural defect.

A class (represented as a folder) is generated for each specific position of the structural defect, and the corresponding response is stored as an image. During this process, the number of images corresponding to each class increases by gradually adjusting the shape or size of structural defects or by introducing random noise to excitation and measurement signals. Once sufficient images have been obtained for each class, the training phase begins using the CNN algorithm. For this work, MATLAB R2022a software is utilized on a desktop equipped with an NVIDIA GeForce RTX 2070 SUPER GPU and an Intel® Core i9 9900K (3.6GHz) CPU with 96GB RAM.

B. CNN ALGORITHM
1) FEATURE EXTRACTION

CNN is effective for image training since it learns in the form of a two-dimensional matrix without compromising the spatial arrangement of data. When a CNN learns from an image, it involves the construction of an appropriate feature map through the convolution operation with a small sized matrix, referred to as a kernel, applied to a two-dimensional matrix corresponding to the input image [46], [47]. During the training process, the weights and biases of the kernel are adjusted and updated to create a feature map that reflects the pattern of the image. This entire process is shown in Fig. 3. The input image is divided into three RGB color channels and zero padding is applied to fill the edges with zeros. Zero padding reduces data loss when the kernel performs a convolution operation. As shown in Eq. (1), a feature map is calculated through an activation function f to a value obtained by adding a bias to a convolution operation of an input image and a kernel. The activation function is essential in enabling the network to learn more features by introducing nonlinearity when stacking layers.

$$x_k^l = f\left(\sum_i w_{ik}^{l-1} * s_i^{l-1} + b_k^l\right) \tag{1}$$

where x_k^l is the k-th feature map in the l-th layer, w_{ik}^{l-1} is the k-th kernel weights connected to the i-th input feature map, s_i^{l-1} is the i-th input feature map, and b_k^l is the k-th bias in the i-th layer.

Among the activation functions, the Rectified Linear Unit (ReLU), the most commonly used in CNNs [48], performs an operation that returns zero if the input value is negative and retains the original value if it is positive. Next, the feature map undergoes subsampling in the max-pooling layer. This step enhances computational efficiency by reducing the spatial dimensions of the feature maps while preserving critical features. The pooled image is then repeated with convolution followed by ReLU and max-pooling to form a feature map with smaller spatial dimensions and increased depth.

2) CLASSIFICATION

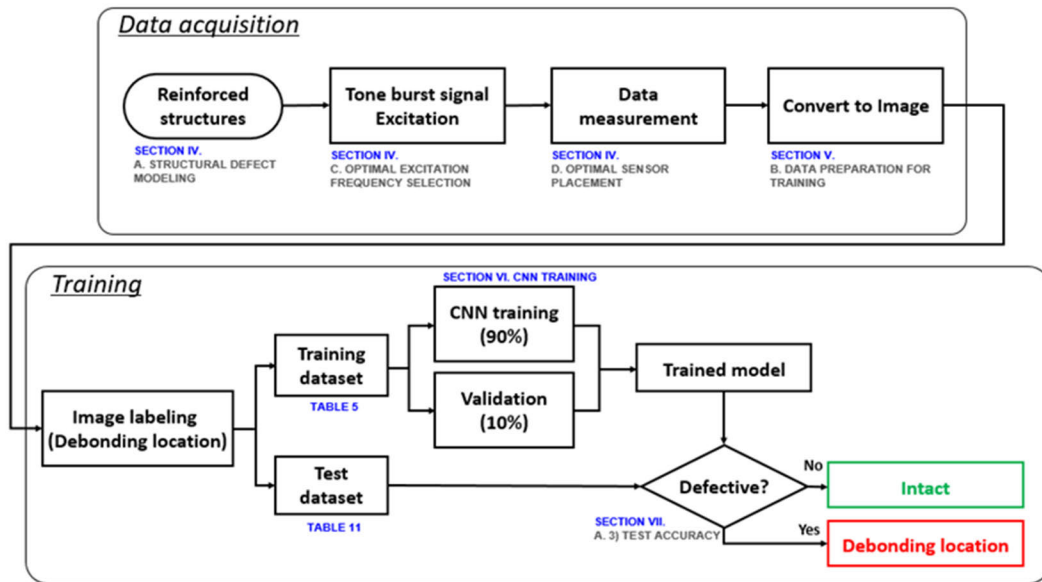For classification, the extracted features are typically represented as one-dimensional vector data. When this one-

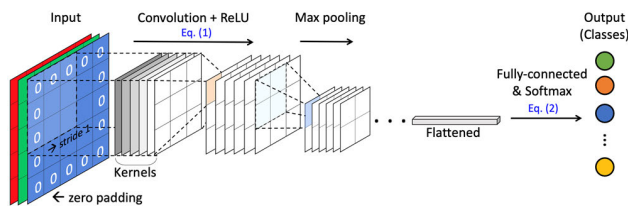**FIGURE 2.** The framework of the proposed method.

FIGURE 3. CNN architecture for image classification.

dimensional feature map is fed into the fully connected layer after learning the last weight and bias. In the output layer, an activation function known as Softmax is employed. As shown in Eq. (2), Softmax calculates the probability distribution Q(x) for each class based on the fully connected vectors x_j^f. This distribution provides a probability score for each class, helping to determine the most likely class for the given input.

$$Q(x) = \frac{exp(x_j^f)}{\sum_{j=1}^{J} exp(x_j^f)} \qquad (2)$$

where j is the index of the output class.

III. EXPERIMENTAL VERIFICATION OF FINITE ELEMENT MODEL

In this chapter, to verify the validity of the finite element model, the group velocity of the Lamb wave is measured and compared with the corresponding value obtained from the FE model. This comparison helps to ensure that the FE model accurately represents the wave propagation characteristics.

A. THEORETICAL GROUP VELOCITY

The dispersion relation of the Lamb wave for an isotropic material is described by Eq. (3) for symmetric modes and Eq. (4) for anti-symmetric modes [49].

$$\frac{tan(qh)}{q} + \frac{tan(ph)\,4k^2 p}{\left(k^2 - q^2\right)^2} = 0 \qquad (3)$$

$$q\,tan(qh) + \frac{tan(ph)\left(k^2 - q^2\right)^2}{4k^2 p} = 0 \qquad (4)$$

$$p^2 = \frac{\omega^2}{c_L^2} - k^2, \quad q^2 = \frac{\omega^2}{c_T^2} - k^2, \quad k = \frac{\omega}{c_p} \qquad (5)$$

$$c_L^2 = \frac{\lambda + 2\mu}{\rho}, \quad c_T^2 = \frac{\mu}{\rho} \qquad (6)$$

where k is the wavenumber, $2h$ is the thickness of the plate, ω is the angular frequency, and μ, λ are Lamé constants. The values of p and q are expressed in Eqs. (5) and (6). For each ωh, the phase velocity, c_p satisfying Eqs. (3) and (4) is obtained, and the group velocity, c_g is calculated using Eq. (7) [49].

$$c_g = \frac{d\omega}{dk} \qquad (7)$$

Hence, to establish the theoretical dispersion relation, it is necessary to have information on density, Poisson's ratio, and Young's modulus for isotropic materials. Density is determined by measuring the weight of the panel using a balance and then dividing it by the volume of the panel. Poisson's ratio is employed as an assumed value, and Young's modulus is experimentally estimated. To achieve this, an accelerometer is attached to an aluminum plate of 400mm × 500mm × 2mm, and the impact hammer test
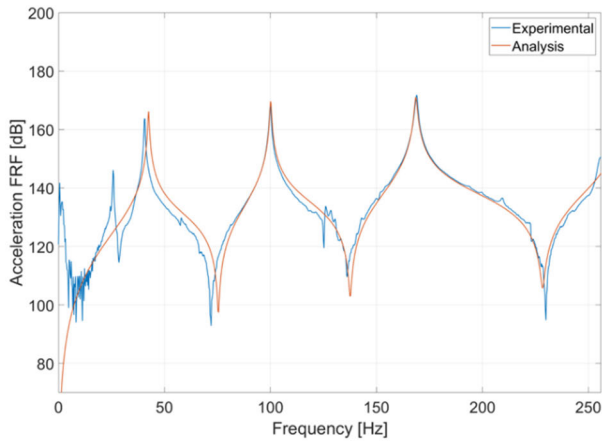
FIGURE 4. Comparison of the experimental FRF and the FRF obtained from the FE analysis when the Young's modulus is 62 GPa.

is performed. The frequency response function (FRF) is measured using a Siemens SCADAS mobile system. Its frequency resolution is set to 0.25 Hz, and the response is measured up to 256 Hz. As shown in Fig. 4, Young's modulus is iteratively adjusted to ensure that the peak of the FRF obtained from FE analysis matches the corresponding peak of the measured FRF. The resulting value for Young's modulus is determined to be 62 GPa. Table 1 provides the parameters necessary for calculating the group velocity and the resultant group velocity curve is shown in Fig. 5.

TABLE 1. Mechanical properties of aluminum plate.

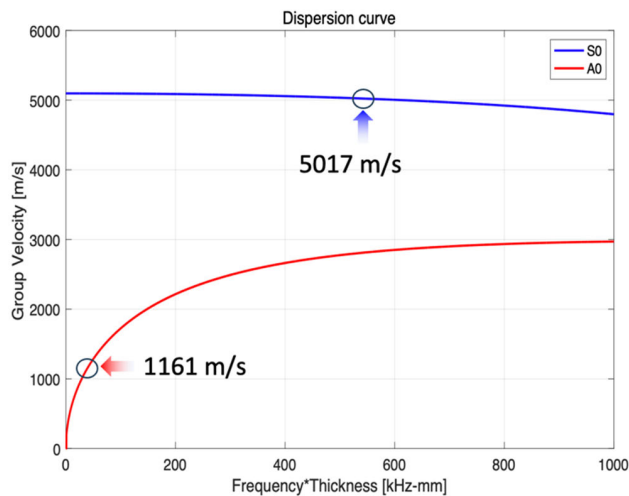| Young's modulus	Mass	Density	Poison's ratio
62 GPa	1075 g	2678.5 kg/m^3	0.33

FIGURE 5. Group velocity dispersion curves for 2 mm aluminum panel.

B. GROUP VELOCITY MEASUREMENT
In order to efficiently measure the group velocities of the A0 mode and the S0 mode, excitation frequencies of 20 kHz for
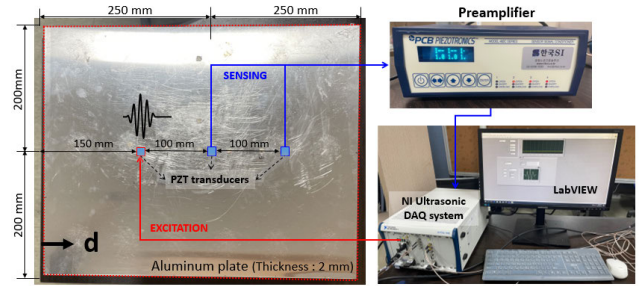

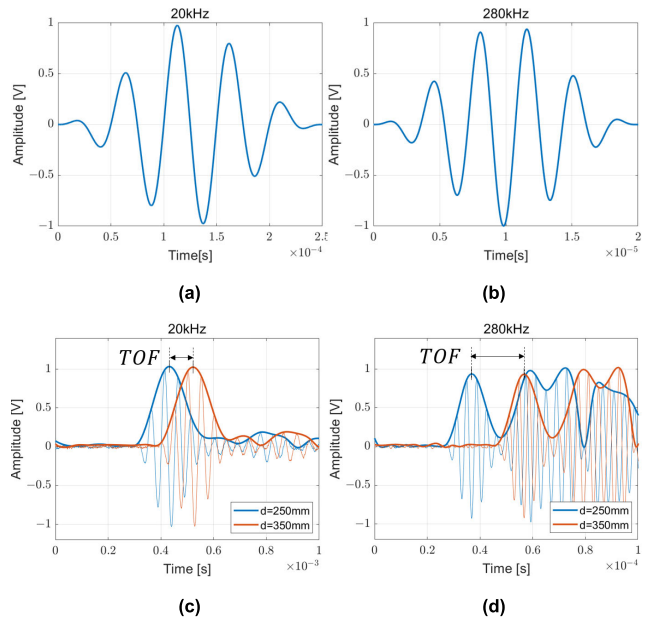**FIGURE 6.** Experiment setup for measuring group velocity.

FIGURE 7. Excitation signals for (a) A0 mode and (b) S0 mode and time-of-flight calculations using Hilbert transformation for (c) A0 mode and (d) S0 mode.

A0 mode and 280 kHz for S0 mode are selected, as both exhibit relatively dominant amplitudes [13].

As illustrated in Fig. 6, the Lamb waves are generated at $d = 150$ mm on the aluminum panel, and subsequent responses are recorded at $d = 250$ mm and $d = 350$ mm. Given the lightweight and thin nature of the PZT wafer, which minimally influences the wave propagation characteristics of the structure [8], the APC-850, manufactured by APC International Ltd., is employed to generate guided waves and detect responses. The digital signals presented in Fig. 7(a) and Fig. 7(b) are generated by the LabVIEW software and then converted into analog signals through the NI-DAQ waveform generator module (NI-PXIe-5423). The converted signals are excited through the PZT actuator, and the resulting responses are captured through the PZT sensors at $d = 250$ mm and $d = 350$ mm. Then, the acquired signal is amplified through the PCB-482C24 signal conditioner to enhance SNR (Signal-to-Noise Ratio). This amplified signal is converted into a digital signal in the oscilloscope module (NI-PXIe-5172).

By applying the Hilbert transformation to the signals at the two locations ($d = 250$ mm, $d = 350$ mm), the time of flight (TOF) can be determined by comparing the time values of the resulting peaks, as described in Fig. 7(c) and Fig. 7(d). Finally, the group velocity is calculated based on the TOF and distance between the two PZT sensors, as defined in Eq. (8).

$$v_g = \frac{distance}{TOF} \qquad (8)$$

TABLE 2. Comparison of group velocities by finite element analysis and experiment.

Frequency	TOF [ms]	v_g [m/s^2] (FE analysis)	v_g [m/s^2] (Experiment)	Error [%]
20kHz	0.0899	1161	1112	4.22
280kHz	0.0197	5017	5070	1.06

Table 2 compares the group velocities obtained from FE analysis and experimental measurements. It is observed that there are errors of about 4% at 20 kHz and around 1% at 280 kHz. The leading cause of this discrepancy is that, unlike the simulation environment, a bonding layer exists to fix the transducer to the panel in the experiment. This bonding layer might have affected the speed of the Lamb wave. In addition, since ultrasonic waves are generated and measured across the entire transducer, the actual wave travel distance could be influenced by the size of the transducer. Therefore, conducting the experiment on a larger panel is expected to decrease the associated error. The comparison of group velocities confirms sufficient similarity between the numerical FE analysis and the experimental value and that reliable insights can be obtained through the FE analysis.

IV. FE SIMULATION

A. STRUCTURAL DEFECT MODELING

Honeycomb sandwich and skin-stringer structures are depicted in Fig. 8, and the mechanical properties information of each part is presented in Table 3. To achieve lightweight reinforcement and optimize strength, the face sheet of the honeycomb sandwich panel and the skin and stringer of the skin-stringer structure were simulated using CFRP composite. To closely mimic real-world structures, the physical properties of WSN3K from SK Chemical were employed [50]. Additionally, the core part of the honeycomb was modeled with 1 mm thick aluminum, a material widely chosen for its cost-effectiveness and ease of processing.

In an intact state, the reinforced structure is joined with a tie condition where the stiffener and the panel are in contact. On the other hand, in areas with structural defects, the structure is in an untied state due to debonding between the stiffener and panel, as shown in Fig. 9(a) and Fig. 9(b). According to the failure analyses of the skin-stringer structure

TABLE 3. Mechanical properties of reinforced structures.

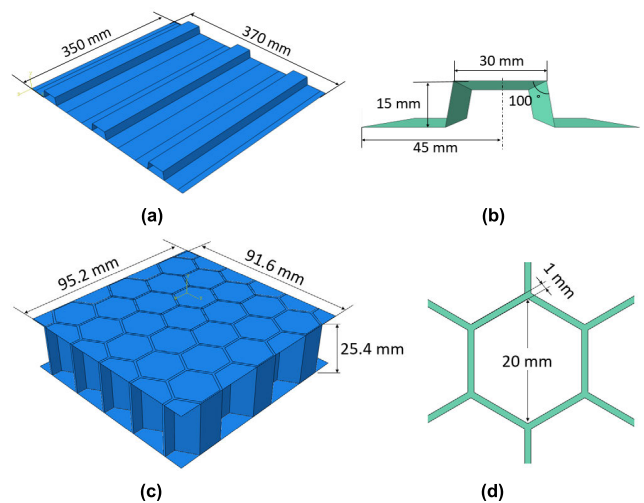| Materials / Properties		CFRP composite[50]	Aluminum
Young's modulus [GPa]	E$_1$	70	
	E$_2$	70	70
	E$_3$	9.6	
Shear modulus [GPa]	G$_{12}$	3.59	
	G$_{13}$	40	-
	G$_{23}$	40	
Poisson's ratio	ν_{12}	0.058	
	ν_{13}	0.058	0.33
	ν_{23}	0.058	
Density [g/mm^3]		1.77×10^{-3}	2.68×10^{-3}
Thickness [mm]		2.1	1
Ply		14 [90˚/45˚/0˚/-45˚/90˚/45˚/0˚/-45˚/90˚/45˚/0˚/-45˚/90˚/45˚]	-
Part		Fig. 8(a) – Skin, Stringer Fig. 8(c) – Face sheet	Fig. 8(c) – Core

FIGURE 8. Geometry information of reinforced panels used in numerical analysis.

subjected to external load [51], [52], [53], it has been noted that the debonding of the stringer starts symmetrically from the inner region. Consequently, the defect in the skin-stringer structure gradually expands from the inner to the outer section of the structure. The defect is modeled by reflecting these characteristics using Abaqus/CAE software.

B. MESH SIZE DETERMINATION

In FE analysis, the size of elements is an essential factor that directly affects the accuracy of the analysis. When the acceleration responses are measured at S1, S2, S3, and S4 with the excitation from the 'Load' location as indicated in Fig. 10, which is the same distance from the excitation
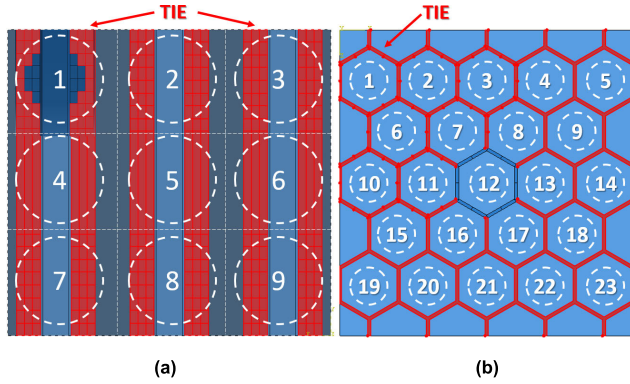
FIGURE 9. Example of structural debonding for (a) skin-stringer panel (See ①) and (b) honeycomb sandwich panel (See ⑫).
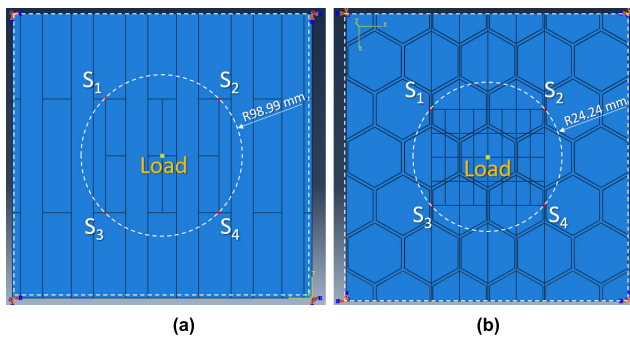

FIGURE 10. Measurement locations at the same distance from the excitation position for (a) skin-stringer panel and (b) honeycomb sandwich panel.

source, the acceleration responses with a coarse element size exhibit discrepancies as shown in Fig. 11, even if the node is positioned as intended. Therefore, the appropriate element size is determined based on the symmetrical distribution of the acceleration response and convergence with a constant value. Stable simulations can be achieved by setting the time increment to 10^{-9} s for the skin-stringer model and 5×10^{-9} s for the honeycomb sandwich panel. With the excitation frequency of 100 kHz, which corresponds to the highest frequency within the frequencies of interest (ranging from 20 kHz to 100 kHz), the responses are measured at S1, S2, S3, and S4 for each element size, and the differences in response (referred to as error) are compared. The error is defined using Eq. (9), where r_i is the response measured at the sensor position S_i.

$$Error = \sum (|r_1 - r_2| + |r_1 - r_3| + |r_1 - r_4| + |r_2 - r_3| \\ + |r_2 - r_4| + |r_3 - r_4|) \quad (9)$$

The calculation results are presented in Fig. 12. In the case of the skin-stringer structure, it is observed that the error is significantly reduced when the mesh size is set to 1 mm. Similarly, for the honeycomb sandwich panel, the error decreases notably when the mesh size is 0.5 mm. With the element sizes set at 1 mm for the skin-stringer structure and 0.5 mm for the honeycomb sandwich panel, respectively,
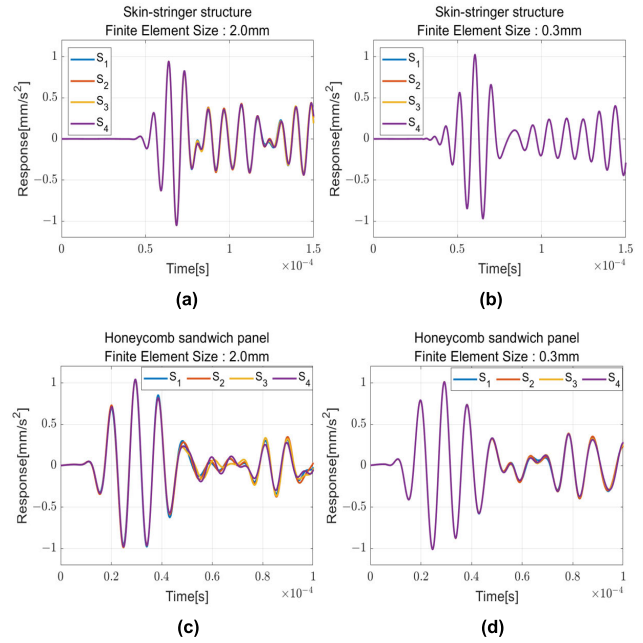

FIGURE 11. Ultrasonic response at 100 kHz at equidistant positions according to each element size for (a) element size: 2.0 mm, skin-stringer structure, (b) element size: 0.3 mm, skin-stringer structure, (c) element size: 2.0 mm, honeycomb sandwich panel, and (d) element size: 0.3 mm, honeycomb sandwich panel.
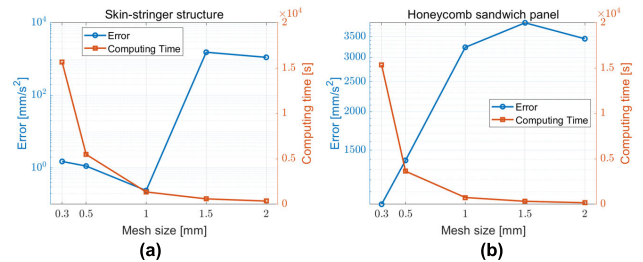

FIGURE 12. Error and calculation time according to mesh size for (a) skin-stringer structure and (b) honeycomb sandwich panel.
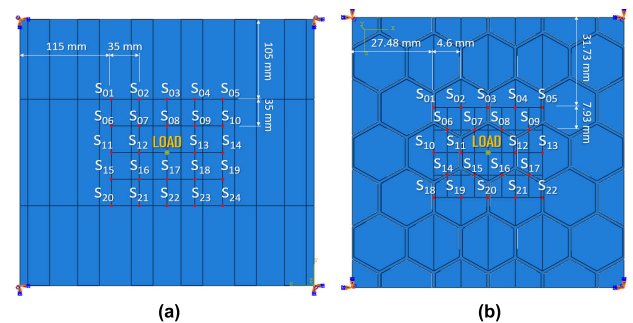

FIGURE 13. Initial sensor positions for (a) skin-stringer panel and (b) honeycomb sandwich panel.

the skin of the skin-stringer structure comprises 129,500 elements, with 399,00 elements per stringer, and the core of the honeycomb sandwich panel is composed of 215,475 elements with 34,615 elements per face sheet.
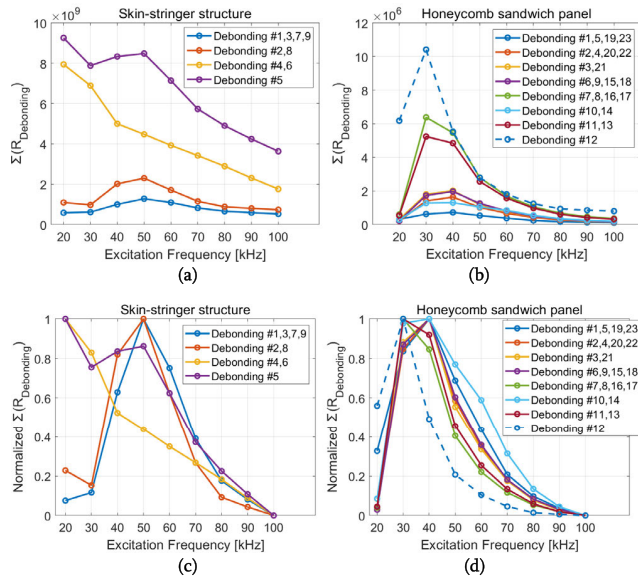
FIGURE 14. Summated scattered wave responses from debonding at each frequency for (a) skin-stringer structure and (b) honeycomb sandwich panel, normalized summated scattered wave responses for (c) skin-stringer structure and (d) honeycomb sandwich panel.

The debonding position index in Fig. 14 corresponds to the positions shown in Fig. 9. Using the symmetry of the structure, it is assumed to have the same value in symmetrical positions. These values are added up according to each frequency and summarized in Table 4. As a result, the optimal excitation frequency for the skin-stringer structure is 50kHz. At the same time, for the honeycomb sandwich panel, it is 40 kHz. These frequencies are expected to generate the highest amplitudes in debonding-induced scattering waves.

TABLE 4. Sum of normalized responses at each frequency for Fig. 14(c) and Fig. 14(d).

Frequency [kHz]	20	30	40	50	60	70	80	90	100
Fig. 14(c)	2.30	1.85	2.81	**3.30**	2.35	1.30	0.68	0.32	0.0
Fig. 14(d)	1.26	7.30	**7.32**	4.17	2.58	1.32	0.58	0.21	0.0

C. OPTIMAL EXCITATION FREQUENCY SELECTION

Among the responses measured by the sensor, the larger the amplitude of the wave scattered by debonding, the clearer the debonding characteristics become, and the debonding classification performance can be improved in the CNN training. Therefore, the excitation frequency should be selected to maximize the amplitude of the wave scattered by debonding. The overall process is as follows.

1) Excite on the central surface ('LOAD' position in Fig. 13) of the intact model (without debonding) and the debonding model using a burst sinusoidal wave with a 20kHz center frequency.
2) Obtain the responses from sensors near the excitation location, as shown in Fig. 13.
3) To extract the debonding-induced scattering wave, calculate the difference between the responses obtained from the intact and the debonded models for each sensor.
4) Apply the absolute value to the debonding-induced scattering waves extracted from all sensors and then sum them to obtain a single representative value.
5) Repeat steps 1) - 4) while changing the debonding position of the debonded model until reaching the final debonding location.
6) Increase the excitation frequency by 10 kHz and iterate through steps 1) - 5) up to 100kHz.

Through the aforementioned process, the sum of the responses scattered from a debonding for each frequency can be computed, as shown in Fig. 14(a) and Fig. 14(b). To ensure an equal contribution for all debonding positions, the summation values for each debonding position are normalized and compared, as shown in Fig. 14(c) and Fig. 14(d).

D. OPTIMAL SENSOR PLACEMENT

The sensor array configuration is established based on the measured signal scattered from debonding, similar to the excitation frequency selection process. Employing a sensor array instead of a single sensor is aimed at extracting debonding characteristics effectively from measured responses. An excessively large number of sensors can introduce responses that are not important for characterizing debonding. This may induce a negative effect, potentially degrading the CNN training performance by reducing the proportion of essential responses in the training data set. Therefore, through the following process, sensors are selectively placed where waves scattered by debonding are measured significantly.

1) Apply a burst sinusoidal wave of 50 kHz for the skin-stringer structure and 40 kHz for the honeycomb sandwich panel to the center surface of both the intact model without debonding and the model simulating debonding at position 1 in Fig. 9.
2) Measure the acceleration response at the candidate sensor locations in Fig. 13 and normalize the values from −1 to 1.
3) To extract the debonding-induced scattering wave, calculate the difference between each sensor's measured responses in the intact and debonded models.
4) Move the debonding position of the debonded model and repeat the steps 1) through 3).
5) Add all the calculated debonding-induced scattering wave values for each debonding position at each sensor (see Fig. 15(a) and Fig. 15 (c)).
6) Sort the values calculated in step 5) in descending order, add them sequentially from largest to smallest, and then divide by the number of data points added. This value represents the average magnitude of the debonding-induced scattering wave measured by one sensor when there are n sensors (see Fig. 15(b) and Fig. 15 (d)).
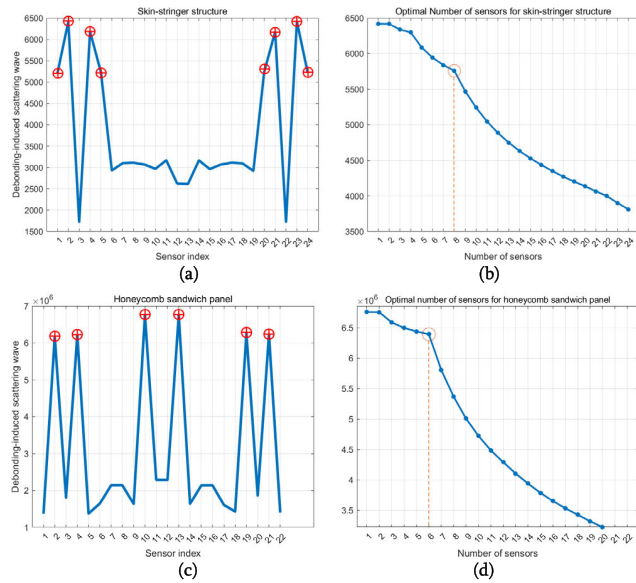
FIGURE 15. Summated scattered wave responses from debonding at each frequency for (a) skin-stringer structure and (b) honeycomb sandwich panel, normalized summated scattered wave responses for (c) skin-stringer structure and (d) honeycomb sandwich panel.
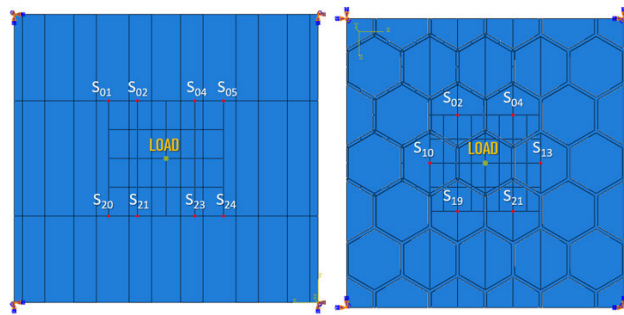

FIGURE 16. Selected sensor locations.

7) From Fig. 15(b) and Fig. 15(d), find the location where the data decreases sharply (large slope), indicating the optimal number of sensors. If the graph sharply declines after n, using only the top n sensors is a viable option to measure more debonding-induced scattering waves relative to the number of sensors used.

The optimal sensor array selected by the above-mentioned procedure is shown in Fig. 16.

V. DATA PREPARATION FOR TRAINING
A. DATA AUGMENTATION METHOD
Based on the specified simulation settings, finite element analysis is performed to simulate various defects. By changing the length and area of debonding, 36 distinct responses for the skin-stringer structure and 108 responses for the honeycomb sandwich panel are generated for each class. Detailed information regarding the debonding geometries is attached in Appendix A and B. Considering the symmetrical nature of the debonding in the skin-stringer model and the initiation of debonding from the inside of the stringer,

it is challenging to obtain enough training data. To address this, additional data is included by adjusting the excitation frequency in 1 kHz increment to supplement the training data for the skin-stringer model.

Since the intact class representing a defect-free state cannot generate various training data, signals with nine surrounding optimal excitation frequencies, excluding the optimal excitation frequency for each model (i.e., 50 kHz for the skin-stringer structure and 40 kHz for the honeycomb sandwich panel) are employed. Hence, in the case of the skin-stringer structure, nine frequencies, excluding 50 kHz, are excited from 45 kHz to 54 kHz with 1 kHz intervals. Similarly, in the honeycomb sandwich panel, nine frequencies are excited at 1 kHz intervals from 35 kHz to 44 kHz, excluding 40 kHz. They are used to increase the data corresponding to the intact class.

To enhance the robustness of the classification model against substantial noise encountered during the measurement, artificial noise is introduced to the original signal. Although this approach may not perfectly simulate noise arising from real devices or boundary conditions, it effectively expands the training database, making extracting critical features of the response easy. The random Gaussian noise is added to the original signal at five different levels (SNR = 8dB, 11dB, 14dB, 17dB, 20dB). The layout for final data augmentation is summarized in Table 5.

TABLE 5. Number of training data for each case.

Classes	Skin-stringer structure		Honeycomb sandwich panel	
	Defective (9)	Intact (1)	Defective (23)	Intact (1)
Debonding types for each class	36 (Appendix A)	-	108 (Appendix B)	-
Excitation signal	3 (49kHz - 51kHz)	9 (45 kHz -49 kHz, 51 kHz -54 kHz)	-	9 (35 kHz -39 kHz, 41 kHz -44 kHz)
Noise level	6 (clear signal, SNR=8dB, 11dB, 14dB, 17dB, 20dB)			
Number of data per class	648	54	648	54

B. PRE-PROCESSING FOR TRAINING
The measured responses of the skin stringer and honeycomb sandwich panel are converted to color bands, stacked in parallel, and employed as a color map image for the training process, as illustrated in Fig. 17. The response is normalized to −1 to 1. Additionally, the DC component is removed using a 9th-order high-pass Butterworth filter, ensuring a more refined and focused dataset for training.

VI. CNN TRAINING
A. CONVOLUTIONAL NEURAL NETWORK MODEL
To effectively train the augmented data, we compare five neural network models such as SqueezeNet [54], GoogLeNet [55], ResNet-101 [56], Inception-ResNet-v2
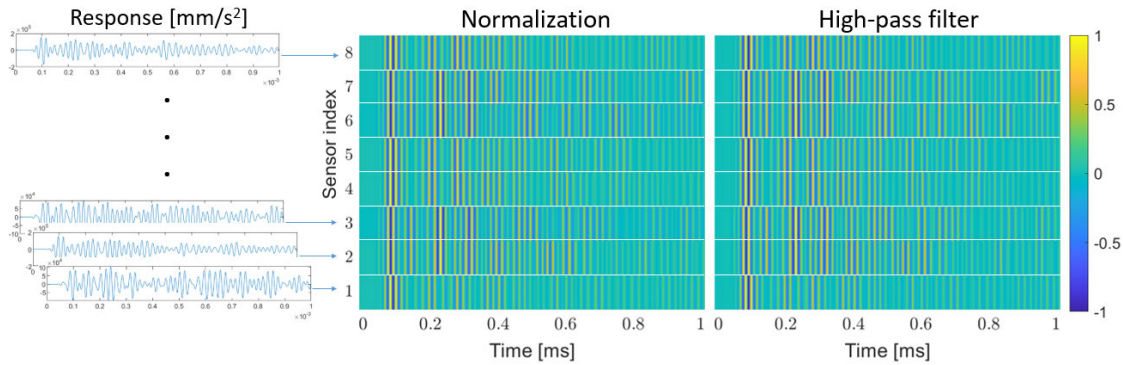
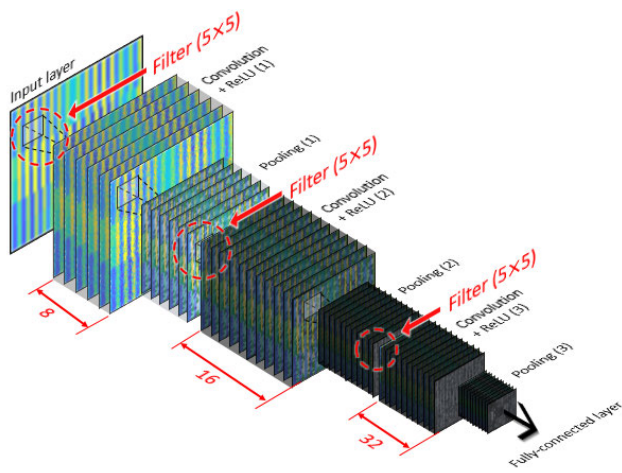**FIGURE 17.** 2D image conversion through stacking of measured signals for applying CNN.

FIGURE 18. Shallow CNN architecture design.

[57], and EfficientNet-b0 [58]. These models are widely and easily implemented by many researchers and developers in deep-learning programming libraries. In addition to these established models, we also incorporate a self-designed shallow neural network. This simple network consists of three convolutional layers and one fully connected layer. As shown in Fig. 18, the structure includes filters of size 5×5, and the convolution layer, ReLU layer, and Max pooling layer are iteratively applied in this design.

1) DATA ASSIGNMENT
Within the dataset, 70% is randomly allocated to the training data, while the remaining 30% is assigned to validation data. The mixture of training and validation data during each epoch facilitates the incorporation of a diverse range of data, enhancing the robustness of the training process.

2) OPTIMIZER
When evaluating the performance of CNN models, the employed optimization algorithm is Stochastic Gradient Descent with Momentum (SGDM). SGDM, an improvement

on the widely used Stochastic Gradient Descent (SGD), addresses the problem of SGD getting trapped in local minima using a momentum term. It introduces an acceleration term, $\gamma (\theta_l - \theta_{l-1})$, that considers the direction and speed of the gradient, enhancing more stable weight updates [57]. The weight update method is as in Eq. 10.

$$\theta_{l+1} = \theta_l - \alpha \nabla E (\theta_l) + \gamma (\theta_l - \theta_{l-1}) \tag{10}$$

where α is the learning rate, γ is the momentum, and $\alpha \nabla E$ is the gradient of the loss function. The default value of 0.9 for momentum is used without modification, and the training rates are all set to 0.001.

3) EARLY STOPPING
The data is divided into a training set to extract image features and a validation set to evaluate the training model at each epoch. The training process continues until validation accuracy converges. However, premature termination before convergence may lead to underfitting, while excessive epochs, even after convergence, may result in overfitting. Therefore, after setting the maximum epoch to 50, if the validation accuracy does not improve for three consecutive epochs, an early termination option is invoked to stop training, ensuring an appropriate number of training iterations. Table 6 shows the convergence time and validation accuracy for each training model applying this approach. In Tables 6 – 8, "S-S" refers to the skin-stringer structure model, and "H-S" denotes the honeycomb sandwich panel model.

B. HYPERPARAMETER TUNING
1) SELECTION OF SIZE AND NUMBER OF FILTERS
As detailed in Table 6, training results using a shallow CNN and transfer learning models show high classification performance, with validation accuracy exceeding 98%. Regarding the convergence speed of validation accuracy, shallow CNN and SqueezeNet exhibit high efficiency. However, considering the superior validation accuracy achieved by

TABLE 6. Performance evaluation of CNN models. (shaded area: fixed-parameters).

CNN Architecture	Depth	Input image size	Training model	Epochs	Elapsed time	Validation accuracy (%)
Shallow CNN	4	539*682	S-S	27	26 min 40 sec	100.00
			H-S	12	30 min 52 sec	98.6824
SqueezeNet	18	227*227	S-S	28	15 min 30 sec	98.1271
			H-S	30	41 min 41 sec	98.3921
GoogLeNet	22	224*224	S-S	23	112 min 15 sec	99.5460
			H-S	16	37 min 32 sec	98.5261
ResNet-101	101	224*224	S-S	12	312 min 42 sec	99.8865
			H-S	16	164 min 15 sec	99.5534
Inception-ResNet-v2	164	299*299	S-S	19	787 min 33 sec	99.6027
			H-S	13	333 min 0 sec	99.3747
EfficientNet-b0	82	224*224	S-S	21	295 min 25 sec	99.9432
			H-S	29	370 min 02 sec	99.8213

TABLE 7. Convolutional kernel optimization.

Size of filter	Number of filters	Training model	Epochs	Elapsed time	Validation accuracy (%)
5×5	4, 8, 16	S-S	27	20 min 12 sec	100.00
		H-S	6	11 min 55 sec	97.3872
	8, 16, 32	S-S	27	26 min 40 sec	100.00
		H-S	75	192 min 75 sec	4.3323
	32, 64, 128	**S-S**	**8**	**9 min 16 sec**	**99.8297**
		H-S	10	30 min 23 sec	98.9951
3×3	4, 8, 16	S-S	27	24 min 5 sec	100.00
		H-S	17	37 min 48 sec	99.3301
	8, 16, 32	S-S	34	32 min 51 sec	100.00
		H-S	**11**	**26 min 46 sec**	**99.0844**
	32, 64, 128	S-S	11	10 min 6 sec	99.9432
		H-S	39	86 min 34 sec	98.6601

TABLE 8. Training performance comparison at different learning rates.

Initial learn rate	Methods	Training model	Epochs	Elapsed time	Validation accuracy (%)
0.005	reducing by 0.5 every 5 epochs	S-S	50	123 min 46 sec	99.9432
0.005		H-S	12	29 min 49 sec	98.5038
0.001		S-S	50	124 min 01 sec	99.9432
0.001		H-S	50	118 min 18 sec	4.3323
	fixed	S-S	11	27 min 17 sec	99.9432
		H-S	13	32 min 09 sec	99.1737
0.0005		S-S	7	18 min 12 sec	100.00
0.0005		H-S	14	34 min 50 sec	99.1291
0.0003		<u>S-S</u>	5	**12 min 43 sec**	<u>99.8865</u>
0.0003		H-S	15	37 min 12 sec	99.3524
0.0001		S-S	7	17 min 27 sec	100.00
0.0001		<u>H-S</u>	12	**29 min 46 sec**	<u>99.5980</u>

errors, leading to consideration of only 3×3 and 5×5 kernel sizes. The convolution layer involves a convolution operation and a zero-padding procedure that fills the edges with zeros. Using odd-sized kernels ensure a stable learning process since the output size matches the input size after passing through the convolution layer. In addition, employing an odd-sized kernel allows data to be evenly distributed according to the central pixel, making it easy to process spatial information efficiently [59], [60].

Table 7 displays the validation accuracy obtained by adjusting the size and number of kernels. In the case of the skin-stringer structure, it shows a high accuracy of around 99%, even for various filter sizes or numbers. Notably, the design attains the fastest convergence of validation accuracy when the filter size is 5×5, and the number of filters increases in the order of 32, 64, and 128. Consequently, the corresponding neural network is selected as the training model for the skin-stringer structure. On the other hand, for the honeycomb sandwich panel, proper training is not achieved in the structure where the filter size is 5×5, and the number of filters increases in the order of 8, 16, and 32, as the validation accuracy remains below 5%. Therefore, a filter size 3×3, which indicates stable validation accuracy, is determined. Among these options, the neural network employing 8, 16, and 32 filters with the swiftest validation accuracy convergence is chosen as the training model for the honeycomb sandwich panel.

2) INITIAL LEARNING RATE
Since the choice of the initial learning rate can impact training time, accuracy, and computational efficiency, it is necessary
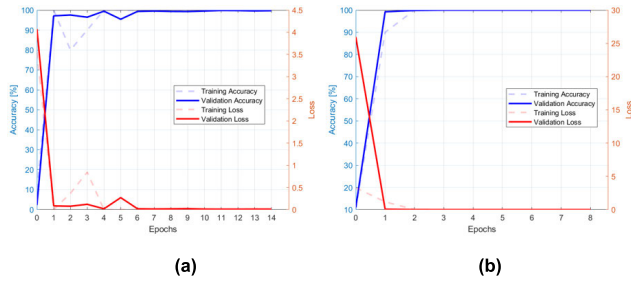
shallow CNN, training with a designed shallow CNN is judged to be more effective.

In a designed shallow neural network, parameters, such as layer order, depth, and kernel, can be freely modified. However, to reduce the number of parameters for the optimization, the depth of the neural network is fixed to 4 (i.e., three hidden layers and one fully connected layer). The hidden layer is structured with a repetition of the convolutional-ReLU-Max pooling layers. Then, optimal values for the size and number of the kernels in the CNN are sought.

The size of the kernel does not necessarily have to be odd, but odd numbers provide the advantage of reducing alignment

FIGURE 19. Training progress for (a)Honeycomb sandwich panel and (b) Skin-stringer structure.

FIGURE 20. 9-fold cross-validation architecture.

to identify the ideal value for the training data through several trials. Learning rate strategies can be categorized into cases where the initial learning rate remains constant throughout training, and the value decreases as training progresses. Training often faced divergence when the initial learning rate was more than 0.01. Therefore, neural networks with the initial learning rate below 0.01 are compared as presented in Table 8. For relatively sizeable initial learning rates of 0.005 and 0.001, the latter strategy, in which the learning rate is reduced by 0.5 times every five epochs, is employed and the learning rate remains fixed during training, from an initial learning rate of 0.001 to the smallest value of 0.0001. In cases where the learning rate dynamically decreases, three out of four models in the comparison group do not terminate early due to the too-small learning rate, and training continues up to the maximum epoch. Their validation accuracies are comparable to those with a fixed learning rate. However, proper training is not conducted under the specific condition (i.e., initial learning rate: 0.001, method: reducing the learning rate by 0.5 times every five epochs) for the honeycomb sandwich panel model. Considering the case of fixed learning rates, both stiffened structures achieved high validation accuracy over 99%. Therefore, the initial learning rates with the fastest convergence are selected to determine a training model with high accuracy and fast convergence (i.e., skin-stringer structure: 0.0003 with fixed rate, honeycomb sandwich panel: 0.0001 with fixed rate). Figure 19 illustrates the training progress under these selected conditions.

C. 9-FOLD CROSS-VALIDATION
This paper employs the k-fold cross-validation technique, a training method that randomly divides the dataset into k folds, designating one as the validation set and the remaining as the training set. This ensures that the validation set is distinct from the training set and undergoes training k times. This approach minimizes training bias towards specific data, providing a more accurate evaluation of the model's general performance [61], [62].

Here, the value of k is set to 9, representing the common divisor of the number of data per class, to maintain an equal balance between validation and training sets in each iteration. The common divisors of 648 (defective dataset) and 54 (intact dataset) are 2, 3, 6, 9, 18, 27, and 54, resulting in
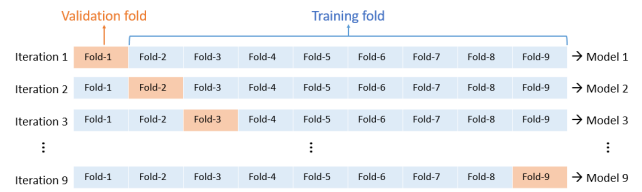
seven potential k-values. However, the choice of the k-value presents a trade-off. If the k-value is small, the number of training models is limited, making it challenging to generalize training results. Conversely, a large k-value may lead to overfitting due to the limited amount of data that can be learned simultaneously. To strike a balance and consider the ratio of training models to training data in each session within the constraints of limited data, we opted for the median value of 9 in this case. The training process is illustrated in Fig. 20, and the averages of the training results across the 9-fold cross-validation sessions are calculated. The training results are detailed in Tables 9 and 10.

TABLE 9. Training result of honeycomb sandwich panel.

Iteration	Epochs	Elapsed time	Validation accuracy (%)	Validation loss
1	12	32 min 50 sec	99.6992	0.0127
2	14	37 min 51 sec	99.5187	0.0152
3	7	19 min 03 sec	98.3755	0.0548
4	16	43 min 20 sec	99.6390	0.0118
5	6	16 min 21 sec	98.3153	0.0619
6	12	32 min 32 sec	99.6390	0.0119
7	11	29 min 51 sec	99.4485	0.0111
8	10	27 min 11 sec	99.1576	0.0278
9	14	37 min 56 sec	99.6992	0.0111
Average	11.33	30 min 46 sec	99.2769	0.0243

TABLE 10. Training result of skin-stringer structure.

Iteration	Epochs	Elapsed time	Validation accuracy (%)	Validation loss
1	7	19 min 43 sec	100.00	9.1139E-10
2	4	11 min 12 sec	99.8471	0.0168
3	15	38 min 50 sec	100.00	1.8228E-10
4	20	52 min 26 sec	99.6942	0.0049
5	6	19 min 57 sec	100.00	7.4550E-8
6	29	88 min 38 sec	99.8471	0.0087
7	5	15 min 51 sec	100.00	7.2911E-10
8	7	19 min 42 sec	100.00	6.9265E-09
9	7	19 min 22 sec	100.00	5.4683E-10
Average	11.11	31 min 44 sec	99.9320	3.38E-3

VII. RESULT
A. CLASSIFICATION PERFORMANCE EVALUATION
Result analysis tools such as confusion matrix, T-SNE, and test accuracy are utilized to evaluate the model's performance comprehensively.
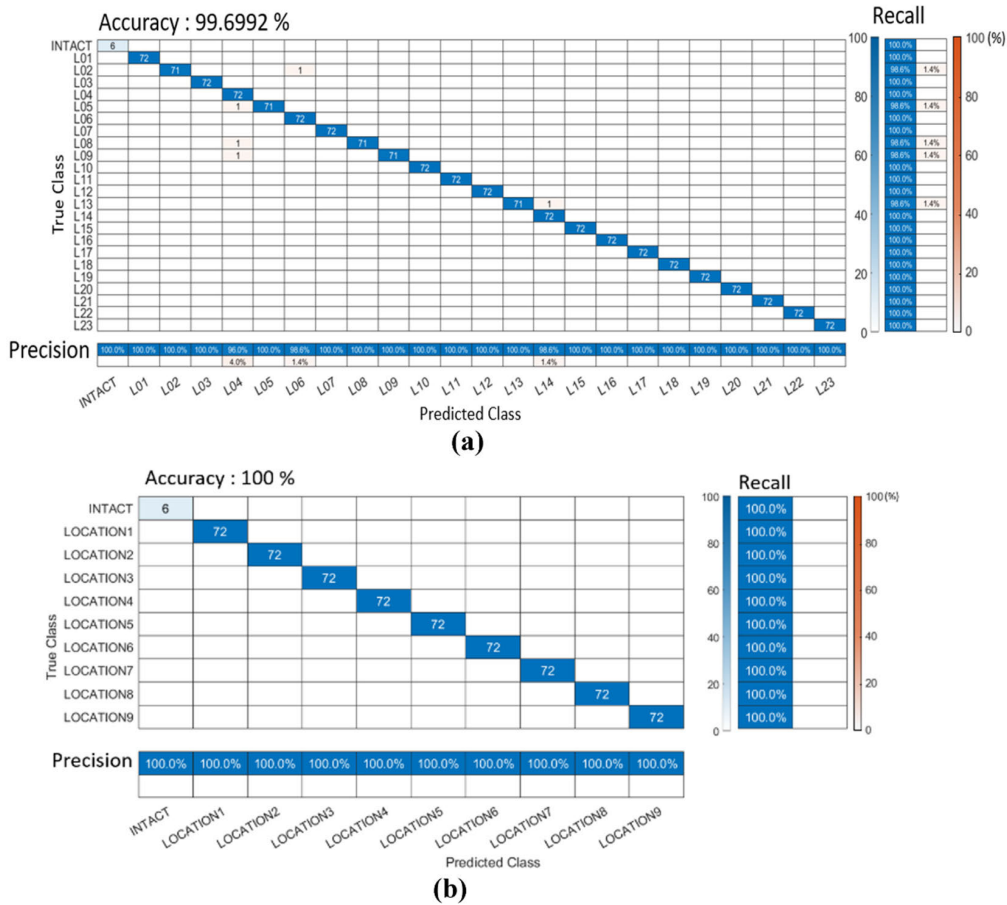
FIGURE 21. Confusion matrix for (a) honeycomb sandwich panel and (b) skin-stringer structure.

1) CONFUSION MATRIX

A confusion matrix serves as an indicator that describes the performance of a classification model. Each row in the matrix represents the true class, while each column corresponds to the predicted class. This matrix can analyze the model's classification capability by counting the number of true positives (TP), true negatives (TN), false positives (FP), and false negatives (FN). The performance evaluation metrics of accuracy, precision, and recall can be calculated using Eqs. 11-13, indicated in Fig. 21.

$$Accuracy = \frac{TP + TN}{TP + TN + FP + FN} \quad (11)$$

$$Precision = \frac{TP}{TP + FP} \quad (12)$$

$$Recall = \frac{TP}{TP + FN} \quad (13)$$

In Fig. 21(a), most classes for honeycomb sandwiches are classified correctly. However, the precision index is slightly lower in the L04 class as 96.0 %, indicating a higher likelihood of errors in misclassification as the L04 class. In the case of skin stringers, the results indicate an optimal classification capability as presented in Fig. 21(b).

2) T-SNE

T-distributed Stochastic Neighbor embedding (T-SNE) is a tool for visualizing data similarity [63]. It facilitates a clearer understanding of the data structure, helping interpret training results. Applying T-SNE to the training model of the honeycomb sandwich panel and skin-stringer structure allows for the confirmation of clusters based on the similarity of the validation data, as shown in Fig. 22.

3) TEST ACCURACY

The evaluation of classification accuracy involves introducing new test data not included in the training or validation sets into the trained model. Specifically, for the defective class, new defect types not utilized in the training or validation sets are employed. For the intact class, new test data is generated by exciting signals not presented in the training data. Adding six noise levels to the new data increases the dataset sixfold. The configuration for the test-data acquisition is summarized in Table 11.

The overall performance and reliability of the trained model are predicted using this collected test data, which has never been utilized in the trained model. The classification accuracy is calculated, as detailed in Table 12. The trained model of the honeycomb sandwich panel classifies new test
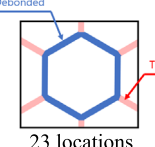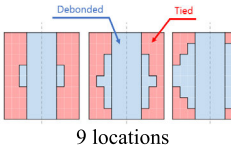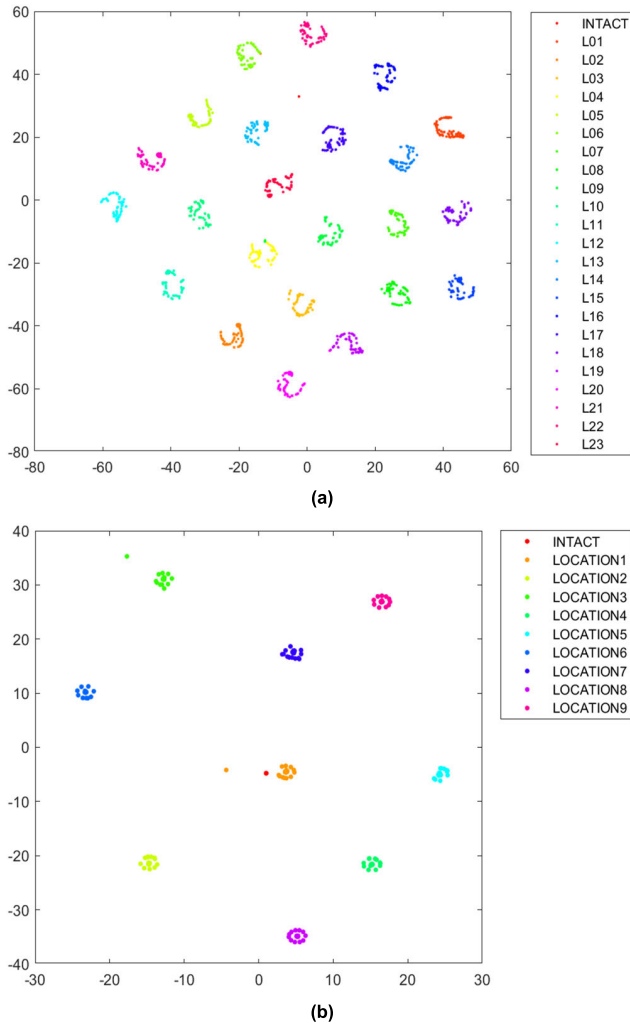
FIGURE 22. T-SNE for (a) Honeycomb sandwich panel (b) Skin-stringer structure.

TABLE 11. Layout for test-data acquisition.

	Honeycomb sandwich panel	Skin-stringer structure
Defective	23 locations	9 locations
Intact	40kHz excitation	50kHz excitation
Noise level	6 (clear signal, SNR=8dB, 11dB, 14dB, 17dB, 20dB)	
Number of classes	24	10
Total number of testing data	144	168

TABLE 12. Test accuracy of honeycomb sandwich panel and skin-stringer structure.

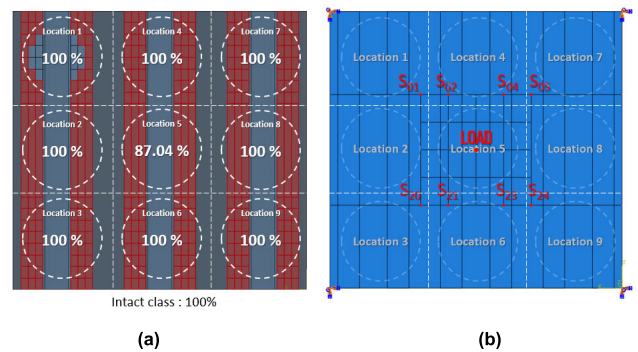| Iteration	Honeycomb sandwich panel	Skin-stringer structure
1	100	100
2	100	100
3	100	97.0238
4	100	100
5	100	96.4286
6	100	97.0238
7	100	97.0238
8	100	100
9	100	100
Average	100	98.6111

FIGURE 23. (a) Classification accuracy corresponding to debonded locations for skin-stringer structures and (b) sensor array location of skin-stringer structures.

data with 100% accuracy in all nine trials, demonstrating remarkable performance and reliability. The trained model of the skin-stringer structure achieves 98.6% accuracy on average, slightly lower than that of the honeycomb sandwich panel. Nonetheless, it still reaches a decent level of performance.

In addition, the distribution of classification accuracy corresponding to each debonding location of the skin-stringer structure is presented in Fig. 23(a). Notably, all misclassifications occur near the sensor array in the 'Location 5' class. As observed in Fig. 23(b), the data from 'Location 5' is a response measured by the sensor array after the excited waves pass through the defect. In other word, when a defect exists in another location, the direct wave is measured without contacting the defect. Then, the effect of the defect is measured at the reflected signal from the defect. Consequently, defect-interaction information is contained in reflected waves propagating opposite to the direction of excited wave propagation. Therefore, the accuracy of the 'Location 5' class is assumed to be lower than that of other classes due to the relative location differences between defects and sensor arrays.

4) CLASSIFICATION ERROR ANALYSIS

To analyze the cause of the imperfect classification accuracy (98.6%) of the skin stringer structure, the classification results are re-organized according to each defect size and noise level. The skin-stringer structure test data encompass defects of three sizes (Small, Medium, and Large) and six
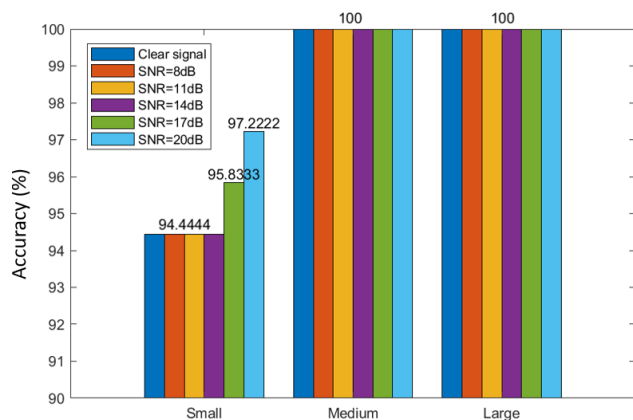
FIGURE 24. Analysis of test accuracy based on defect size and noise levels for skin-stringer structure.

noise levels (Clear signal, SNR=8dB, 11dB, 14dB, 17dB, 20dB), detailed in Table 11 and Appendix A. Subsequently, the test results were segmented according to defect size and noise level, as illustrated in Fig. 24.

The average accuracy within the 'Small' group was 95.14 %, noticeably lower than that of other groups, which achieved 100% classification accuracy. This means that as the defect's size increases, the signal change due to the defect becomes more evident, making it more advantageous to classify the location of the defect. Within the 'Small' group, accuracy appears to increase with higher SNR levels when solely considering noise levels. However, the classification accuracy for the clear signal without noise is low, indicating a substantial impact of data noise on classification results. In conclusion, defect size affects classification performance more significantly than the noise level.

VIII. CONCLUSION

In this study, we have introduced a method that employs a CNN-based non-destructive evaluation algorithm to remotely detect and classify debonding damage in honeycomb sandwich panels and skin-stringer structures, which are commonly used in aerospace structures. The research process includes identification of the optimal strategy from data collection to the derivation of training results. Considering significant cost and time limitations in actually manufacturing reinforced structures with various debonding, acquiring a substantial number of samples for CNN application becomes challenging. To address this limitation, we used finite element models of stiffened structures to collect sufficient data to conduct deep learning training on debonding defects and have checked the methodological effectiveness.

To maximize the information derived from defects, the excitation frequency was selected based on the amplitude of the reflected wave from each defect. Additionally, the optimal location and number of ultrasonic sensors were determined based this criterion. The collected time data from the optimal sensor array were then stacked vertically and expressed as 2D figures. Subsequently, the defect locations were labeled, and

a CNN was trained. To enhance classification performance, the amount of training data was increased by introducing variations in the shape, size of defects, and noise levels. Consequently, 648 training data were gathered for each defective class, along with 54 instances for each intact class, for both honeycomb sandwich panel and skin-stringer structures.

We compared six CNN-based transfer learning models and a custom-designed shallow neural network to select a better training model. Our findings demonstrated that the customized-shallow CNN showed not only rapid convergence in validate accuracy but also achieved a sufficiently high level of performance. We optimized the kernel and learning rate using a trial-and-error approach to enhance the classification accuracy further and fast convergence in the shallow neural network. Consequently, we obtained a tailored neural network optimization for each honeycomb sandwich panel and skin-stringer structure. We opted for a fixed initial learning rate among the various training options to expedite the training process. An appropriate learning rate was also determined through the trial-and-error method. We mitigate underfitting and overfitting by introducing an early termination option that terminates training if the verification accuracy does not improve for three epochs. The 9-fold cross-validation method is used to minimize data bias. The training result indicated an average validation accuracy of 99.28 % for the honeycomb sandwich panel and 99.93 % for the skin-stringer structure.

To evaluate the training results in detail, we employed a confusion matrix and three classification performance evaluation indicators, and the classification results were visualized through T-SNE. Subsequently, the general performance of the trained model was assessed using new test data not included in the training dataset. As a result, the honeycomb sandwich panel achieved an average classification accuracy of 100%, and the skin-stringer structure attained an average classification accuracy of 98.61%, indicating high reliability for the training model. Furthermore, more research was conducted on the corresponding classification errors of skin-stringer structure. Using the new test data, we explored the effects of defect size and noise level on defect classification. The test results indicated no significant effect of noise level, and the small size of defect among the test data exhibited a classification accuracy of about 4.91% lower than other sizes.

In this study, except for the experiment to verify the finite element model, the design and verification of the algorithm were all based on finite element analysis. It is essential to note that certain factors inherent to real-world measurements, such as unforeseen environmental changes or noise, may not have been comprehensively considered. Consequently, to address these limitations, subsequent research endeavors should validate the outcomes through experimentation with actual samples or aerospace structures. This approach will provide a more robust assessment of the algorithm's performance in practical scenarios and enhance the applicability of the findings.
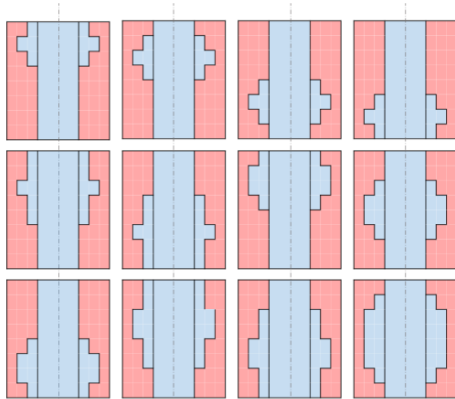
APPENDIX A
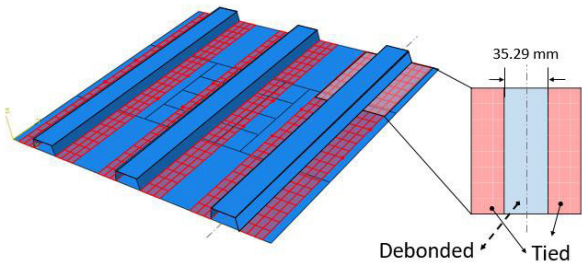
< Debonding-defect configurations of skin-stringer panel >
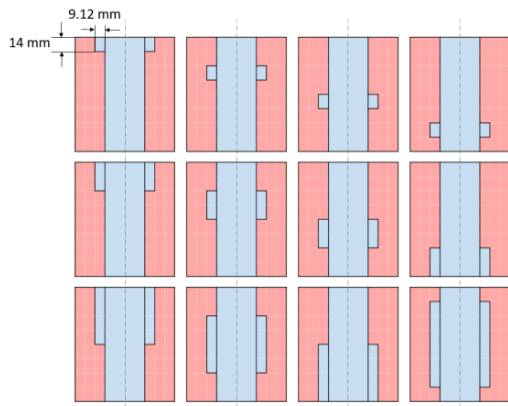
< Small-sized defect group >

< Medium-sized defect group >

< Large-sized defect group >

APPENDIX B

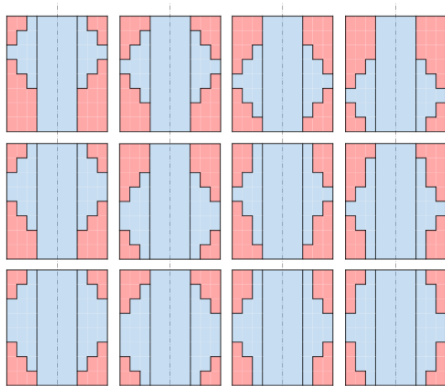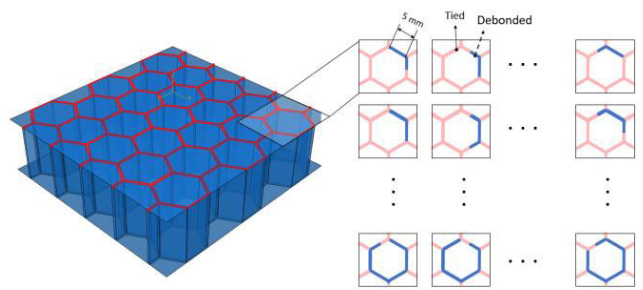< Debonding-defect configurations of honeycomb sandwich panels >

REFERENCES

[1] H. Towsyfyan, A. Biguri, R. Boardman, and T. Blumensath, "Successes and challenges in non-destructive testing of aircraft composite structures," *Chin. J. Aeronaut.*, vol. 33, no. 3, pp. 771–791, Mar. 2020, doi: 10.1016/j.cja.2019.09.017.

[2] T. D'Orazio, M. Leo, A. Distante, C. Guaragnella, V. Pianese, and G. Cavaccini, "Automatic ultrasonic inspection for internal defect detection in composite materials," *NDT E Int.*, vol. 41, no. 2, pp. 145–154, Mar. 2008, doi: 10.1016/j.ndteint.2007.08.001.

[3] J. Dong, B. Kim, A. Locquet, P. McKeon, N. Declercq, and D. S. Citrin, "Nondestructive evaluation of forced delamination in glass fiber-reinforced composites by terahertz and ultrasonic waves," *Compos. B, Eng.*, vol. 79, pp. 667–675, Sep. 2015, doi: 10.1016/j.compositesb.2015.05.028.

[4] C. Garnier, M.-L. Pastor, F. Eyma, and B. Lorrain, "The detection of aeronautical defects in situ on composite structures using non destructive testing," *Compos. Struct.*, vol. 93, no. 5, pp. 1328–1336, Apr. 2011, doi: 10.1016/j.compstruct.2010.10.017.

[5] D. G. Aggelis and T. Shiotani, "Repair evaluation of concrete cracks using surface and through-transmission wave measurements," *Cement Concrete Compos.*, vol. 29, no. 9, pp. 700–711, Oct. 2007, doi: 10.1016/j.cemconcomp.2007.05.001.

[6] A. A. Shah and Y. Ribakov, "Non-destructive evaluation of concrete in damaged and undamaged states," *Mater. Des.*, vol. 30, no. 9, pp. 3504–3511, Oct. 2009, doi: 10.1016/j.matdes.2009.03.008.

[7] J. Moll, R. T. Schulte, B. Hartmann, C.-P. Fritzen, and O. Nelles, "Multi-site damage localization in anisotropic plate-like structures using an active guided wave structural health monitoring system," *Smart Mater. Struct.*, vol. 19, no. 4, Mar. 2010, Art. no. 045022, doi: 10.1088/0964-1726/19/4/045022.

[8] M. Mitra and S. Gopalakrishnan, "Guided wave based structural health monitoring: A review," *Smart Mater. Struct.*, vol. 25, no. 5, Mar. 2016, Art. no. 053001, doi: 10.1088/0964-1726/25/5/053001.

[9] F. Ricci, E. Monaco, N. D. Boffa, L. Maio, and V. Memmolo, "Guided waves for structural health monitoring in composites: A review and implementation strategies," *Prog. Aerosp. Sci.*, vol. 129, Feb. 2022, Art. no. 100790, doi: 10.1016/j.paerosci.2021.100790.

[10] H. Lamb, "On waves in an elastic plate," *Proc. Royal Soc. London. Ser. A, Containing Papers Math. Phys. Character*, vol. 93, no. 648, pp. 114–128, Jan. 1997, doi: 10.1098/rspa.1917.0008.

[11] C. Valle and J. W. Littles, "Flaw localization using the reassigned spectrogram on laser-generated and detected Lamb modes," *Ultrasonics*, vol. 39, no. 8, pp. 535–542, Jun. 2002, doi: 10.1016/s0041-624x(02)00249-4.

[12] D. N. Alleyne and P. Cawley, "The interaction of Lamb waves with defects," *IEEE Trans. Ultrason., Ferroelectr., Freq. Control*, vol. 39, no. 3, pp. 381–397, May 1992, doi: 10.1109/58.143172.

[13] J.-H. Han and Y.-J. Kim, "Time–frequency beamforming for nondestructive evaluations of plate using ultrasonic Lamb wave," *Mech. Syst. Signal Process.*, vols. 54–55, pp. 336–356, Mar. 2015, doi: 10.1016/j.ymssp.2014.09.008.

[14] R. K. Ing and M. Fink, "Time-reversed Lamb waves," *IEEE Trans. Ultrason., Ferroelectr., Freq. Control*, vol. 45, no. 4, pp. 1032–1043, Jul. 1998, doi: 10.1109/58.710586.

[15] S. M. Prasad, K. Balasubramaniam, and C. V. Krishnamurthy, "Structural health monitoring of composite structures using Lamb wave tomography," *Smart Mater. Struct.*, vol. 13, no. 5, pp. N73–N79, Jul. 2004, doi: 10.1088/0964-1726/13/5/n01.

[16] A. Baltazar, C. D. Hernandez-Salazar, and B. Manzanares-Martinez, "Study of wave propagation in a multiwire cable to determine structural damage," *NDT E Int.*, vol. 43, no. 8, pp. 726–732, Nov. 2010, doi: 10.1016/j.ndteint.2010.08.007.

[17] F. Li, Z. Su, L. Ye, and G. Meng, "A correlation filtering-based matching pursuit (CF-MP) for damage identification using Lamb waves," *Smart Mater. Struct.*, vol. 15, no. 6, pp. 1585–1594, Oct. 2006, doi: 10.1088/0964-1726/15/6/010.

[18] H. Kim and F.-G. Yuan, "Adaptive signal decomposition and dispersion removal based on the matching pursuit algorithm using dispersion-based dictionary for enhancing damage imaging," *Ultrasonics*, vol. 103, Apr. 2020, Art. no. 106087, doi: 10.1016/j.ultras.2020.106087.

[19] H. Sohn, G. Park, J. R. Wait, N. P. Limback, and C. R. Farrar, "Wavelet-based active sensing for delamination detection in composite structures," *Smart Mater. Struct.*, vol. 13, no. 1, pp. 153–160, Feb. 2004, doi: 10.1088/0964-1726/13/1/017.

[20] S. Legendre, D. Massicotte, J. Goyette, and T. K. Bose, "Wavelet-transform-based method of analysis for Lamb-wave ultrasonic NDE signals," *IEEE Trans. Instrum. Meas.*, vol. 49, no. 3, pp. 524–530, Jun. 2000, doi: 10.1109/19.850388.

[21] R. Latif, E. H. Aassif, G. Maze, A. Moudden, and B. Faiz, "Determination of the group and phase velocities from time–frequency representation of Wigner–Ville," *NDT E Int.*, vol. 32, no. 7, pp. 415–422, Oct. 1999, doi: 10.1016/s0963-8695(99)00013-4.

[22] D. Dai and Q. He, "Structure damage localization with ultrasonic guided waves based on a time–frequency method," *Signal Process.*, vol. 96, pp. 21–28, Mar. 2014, doi: 10.1016/j.sigpro.2013.05.025.

[23] A. Demma, P. Cawley, M. Lowe, A. G. Roosenbrand, and B. Pavlakovic, "The reflection of guided waves from notches in pipes: A guide for interpreting corrosion measurements," *NDT E Int.*, vol. 37, no. 3, pp. 167–180, Apr. 2004, doi: 10.1016/j.ndteint.2003.09.004.

[24] R. Guan, Y. Lu, W. Duan, and X. Wang, "Guided waves for damage identification in pipeline structures: A review," *Struct. Control Health Monitor.*, vol. 24, no. 11, p. e2007, Nov. 2017, doi: 10.1002/stc.2007.

[25] K. Diamanti, C. Soutis, and J. M. Hodgkinson, "Lamb waves for the non-destructive inspection of monolithic and sandwich composite beams," *Compos. A, Appl. Sci. Manuf.*, vol. 36, no. 2, pp. 189–195, Feb. 2005, doi: 10.1016/j.compositesa.2004.06.013.

[26] Z. Su, C. Yang, N. Pan, L. Ye, and L. Zhou, "Assessment of delamination in composite beams using shear horizontal (SH) wave mode," *Compos. Sci. Technol.*, vol. 67, no. 2, pp. 244–251, Feb. 2007, doi: 10.1016/j.compscitech.2006.08.019.

[27] N. Bourasseau, E. Moulin, C. Delebarre, and P. Bonniau, "Radome health monitoring with Lamb waves: Experimental approach," *NDT E Int.*, vol. 33, no. 6, pp. 393–400, Sep. 2000, doi: 10.1016/s0963-8695(00)00007-4.

[28] S. M. H. Hosseini and U. Gabbert, "Numerical simulation of the Lamb wave propagation in honeycomb sandwich panels: A parametric study," *Compos. Struct.*, vol. 97, pp. 189–201, Mar. 2013, doi: 10.1016/j.compstruct.2012.09.055.

[29] H. Baid, C. Schaal, H. Samajder, and A. Mal, "Dispersion of Lamb waves in a honeycomb composite sandwich panel," *Ultrasonics*, vol. 56, pp. 409–416, Feb. 2015, doi: 10.1016/j.ultras.2014.09.007.

[30] A. Spada, M. Capriotti, and F. L. di Scalea, "Global-local model for guided wave scattering problems with application to defect characterization in built-up composite structures," *Int. J. Solids Struct.*, vols. 182–183, pp. 267–280, Jan. 2020, doi: 10.1016/j.ijsolstr.2019.08.015.

[31] L. Xu, Y. Su, K. Wang, X. Yang, S. Yuan, and Z. Su, "An elastodynamic reciprocity theorem-based closed-form solution to second harmonic generation of Lamb waves by a fatigue crack: Theory & experimental validation," *J. Sound Vibrat.*, vol. 509, Sep. 2021, Art. no. 116226, doi: 10.1016/j.jsv.2021.116226.

[32] N. Chakraborty, V. T. Rathod, D. Roy Mahapatra, and S. Gopalakrishnan, "Guided wave based detection of damage in honeycomb core sandwich structures," *NDT E Int.*, vol. 49, pp. 27–33, Jul. 2012, doi: 10.1016/j.ndteint.2012.03.008.

[33] K. Zheng, Z. Li, Z. Ma, J. Chen, J. Zhou, and X. Su, "Damage detection method based on Lamb waves for stiffened composite panels," *Compos. Struct.*, vol. 225, Oct. 2019, Art. no. 111137, doi: 10.1016/j.compstruct.2019.111137.

[34] S. Sikdar and S. Banerjee, "Identification of disbond and high density core region in a honeycomb composite sandwich structure using ultrasonic guided waves," *Compos. Struct.*, vol. 152, pp. 568–578, Sep. 2016, doi: 10.1016/j.compstruct.2016.05.064.

[35] F. Gao, L. Wang, J. Hua, J. Lin, and A. Mal, "Application of Lamb wave and its coda waves to disbond detection in an aeronautical honeycomb composite sandwich," *Mech. Syst. Signal Process.*, vol. 146, Jan. 2021, Art. no. 107063, doi: 10.1016/j.ymssp.2020.107063.

[36] S. Yashiro, J. Takatsubo, and N. Toyama, "An NDT technique for composite structures using visualized Lamb-wave propagation," *Compos. Sci. Technol.*, vol. 67, nos. 15–16, pp. 3202–3208, Dec. 2007, doi: 10.1016/j.compscitech.2007.04.006.

[37] Y. Gao, X. Li, X. V. Wang, L. Wang, and L. Gao, "A review on recent advances in vision-based defect recognition towards industrial intelligence," *J. Manuf. Syst.*, vol. 62, pp. 753–766, Jan. 2022, doi: 10.1016/j.jmsy.2021.05.008.

[38] V. Nasteski, "An overview of the supervised machine learning methods," *Horizons*, vol. 4, pp. 51–62, Dec. 2017, doi: 10.20544/HORIZONS.B.04.1.17.P05.

[39] A. De Fenza, A. Sorrentino, and P. Vitiello, "Application of artificial neural networks and probability ellipse methods for damage detection using Lamb waves," *Compos. Struct.*, vol. 133, pp. 390–403, Dec. 2015, doi: 10.1016/j.compstruct.2015.07.089.

[40] K. Virupakshappa and E. Oruklu, "Ultrasonic flaw detection using support vector machine classification," in *Proc. IEEE Int. Ultrason. Symp. (IUS)*, Oct. 2015, pp. 1–4, doi: 10.1109/ULTSYM.2015.0128.

[41] I. Tabian, H. Fu, and Z. S. Khodaei, "A convolutional neural network for impact detection and characterization of complex composite structures," *Sensors*, vol. 19, no. 22, p. 4933, Nov. 2019, doi: 10.3390/s19224933.

[42] H. Liu and Y. Zhang, "Deep learning based crack damage detection technique for thin plate structures using guided Lamb wave signals," *Smart Mater. Struct.*, vol. 29, no. 1, Dec. 2019, Art. no. 015032, doi: 10.1088/1361-665x/ab58d6.

[43] J.-Y. Kim and J.-H. Han, "Optimal transducer placement for deep learning-based non-destructive evaluation," *Sensors*, vol. 23, no. 3, p. 1349, Jan. 2023, doi: 10.3390/s23031349.

[44] Y. Liao, X. Qing, Y. Wang, and F. Zhang, "Damage localization for composite structure using guided wave signals with gramian angular field image coding and convolutional neural networks," *Compos. Struct.*, vol. 312, May 2023, Art. no. 116871, doi: 10.1016/j.compstruct.2023.116871.

[45] N. Munir, H.-J. Kim, J. Park, S.-J. Song, and S.-S. Kang, "Convolutional neural network for ultrasonic weldment flaw classification in noisy conditions," *Ultrasonics*, vol. 94, pp. 74–81, Apr. 2019, doi: 10.1016/j.ultras.2018.12.001.

[46] S. Albawi, T. A. Mohammed, and S. Al-Zawi, "Understanding of a convolutional neural network," in *Proc. Int. Conf. Eng. Technol. (ICET)*, Aug. 2017, pp. 1–6, doi: 10.1109/ICEngTechnol.2017.8308186.

[47] J. Gu, Z. Wang, J. Kuen, L. Ma, A. Shahroudy, B. Shuai, T. Liu, X. Wang, G. Wang, J. Cai, and T. Chen, "Recent advances in convolutional neural networks," *Pattern Recognit.*, vol. 77, pp. 354–377, May 2018, doi: 10.1016/j.patcog.2017.10.013.

[48] K. He, X. Zhang, S. Ren, and J. Sun, "Delving deep into rectifiers: Surpassing human-level performance on ImageNet classification," in *Proc. IEEE Int. Conf. Comput. Vis. (ICCV)*, Dec. 2015, pp. 1026–1034, doi: 10.1109/ICCV.2015.123.

[49] J. L. Rose, *Ultrasonic Waves in Solid Media*. Cambridge, U.K.: Cambridge Univ. Press, 1999.

[50] Y.-B. Park, K.-H. Nguyen, J.-H. Kweon, J.-H. Choi, and J.-S. Han, "Structural analysis of a composite target-drone," *Int. J. Aeronaut. Space Sci.*, vol. 12, no. 1, pp. 84–91, Mar. 2011, doi: 10.5139/ijass.2011.12.1.84.

[51] J. Bertolini, B. Castanié, J.-J. Barrau, and J.-P. Navarro, "An experimental and numerical study on Omega stringer debonding," *Compos. Struct.*, vol. 86, nos. 1–3, pp. 233–242, Nov. 2008, doi: 10.1016/j.compstruct.2008.03.013.

[52] R. Vescovini, C. G. Dávila, and C. Bisagni, "Failure analysis of composite multi-stringer panels using simplified models," *Compos. B, Eng.*, vol. 45, no. 1, pp. 939–951, Feb. 2013, doi: 10.1016/j.compositesb.2012.07.030.

[53] B. Li, Y. Gong, Y. Gao, M. Hou, and L. Li, "Failure analysis of hat-stringer-stiffened aircraft composite panels under four-point bending loading," *Materials*, vol. 15, no. 7, p. 2430, Mar. 2022, doi: 10.3390/ma15072430.

[54] F. N. Iandola, S. Han, M. W. Moskewicz, K. Ashraf, W. J. Dally, and K. Keutzer, "SqueezeNet: AlexNet-level accuracy with 50x fewer parameters and <0.5MB model size," Nov. 2016, *arXiv:1602.07360*.

[55] B. Zhou, A. Khosla, A. Lapedriza, A. Torralba, and A. Oliva, "Places: An image database for deep scene understanding," 2016, *arXiv:1610.02055*.

[56] K. He, X. Zhang, S. Ren, and J. Sun, "Deep residual learning for image recognition," in *Proc. IEEE Conf. Comput. Vis. Pattern Recognit. (CVPR)*, Jun. 2016, pp. 770–778, doi: 10.1109/CVPR.2016.90.

[57] C. Szegedy, S. Ioffe, V. Vanhoucke, and A. Alemi, "Inception-v4, Inception-ResNet and the impact of residual connections on learning," in *Proc. AAAI Conf. Artif. Intell.*, vol. 31, no. 1, Feb. 2017, Art. no. 1, doi: 10.1609/aaai.v31i1.11231.

[58] M. Tan and Q. Le, "EfficientNet: Rethinking model scaling for convolutional neural networks," in *Proc. 36th Int. Conf. Mach. Learn.*, May 2019, pp. 6105–6114.

[59] C. Peng, X. Zhang, G. Yu, G. Luo, and J. Sun, "Large kernel matters— Improve semantic segmentation by global convolutional network," in *Proc. IEEE Conf. Comput. Vis. Pattern Recognit. (CVPR)*, Jul. 2017, pp. 1743–1751.

[60] X. Wu, S. Wu, X. Tian, X. Guo, and X. Luo, "Effects of hyperparameters on flow field reconstruction around a foil by convolutional neural networks," *Ocean Eng.*, vol. 247, Mar. 2022, Art. no. 110650, doi: 10.1016/j.oceaneng.2022.110650.

[61] M. W. Browne, "Cross-validation methods," *J. Math. Psychol.*, vol. 44, no. 1, pp. 108–132, Mar. 2000, doi: 10.1006/jmps.1999.1279.

[62] D. Anguita, L. Ghelardoni, A. Ghio, L. Oneto, and S. Ridella, "The 'K' in K-fold cross validation," in *Proc. Eur. Symp. Artif. Neural Netw. (ESANN)*, Apr. 2012, pp. 441–446.

[63] L. Van der Maaten and G. Hinton, "Visualizing data using t-SNE," *J. Mach. Learn. Res.*, vol. 9, no. 11, pp. 1–27, 2008.

YOUNGKI KIM (Senior Member, IEEE) received the B.S. and M.S. degrees in mechanical engineering from Seoul National University, South Korea, in 2001 and 2003, respectively, and the Ph.D. degree in mechanical engineering from the University of Michigan, Ann Arbor, MI, USA, in 2014.

He is currently an Assistant Professor with the Department of Mechanical Engineering, University of Michigan–Dearborn (UM-Dearborn), Dearborn. Prior to joining UM-Dearborn, he was a Research Engineer with the Ann Arbor Technical Center, Southwest Research Institute, from 2015 to 2017. From 2003 to 2008, he was with Hyundai-Kia Motor Company as a Research Engineer. His research interests include modeling and estimation/control of dynamic systems in automotive and energy storage systems.

Dr. Kim was a recipient of the SAE Russell S. Springer Award from the SAE International, in 2019.

JI-YUN KIM received the B.S. degree in mechanical engineering from the Tech University of Korea, Siheung-si, South Korea, in 2022, where she is currently pursuing the M.S. degree in mechanical engineering. Her research interest includes deep learning-based non-destructive evaluation.

JE-HEON HAN (Member, IEEE) received the B.S. degree from Korea University, Seoul, South Korea, in 2000, the M.S. degree from Seoul National University, Seoul, in 2003, and the Ph.D. degree in mechanical engineering from Texas A&M University, College Station, TX, USA, in 2013. From 2003 to 2009, he was an NVH Development Engineer with the Hyundai-Kia Research and Development Center and a Senior Engineer with the Korea Aerospace Research Institute, from 2014 to 2016. Since 2016, he has been an Assistant/Associate Professor with the Department of Mechanical Engineering, Tech University of Korea, Siheung-si, South Korea. His research interests include acoustic analysis, array signal processing, non-destructive evaluation, and mechanical system design using CAE software.

● ● ●